ADVANCED ELECTRONIC MATERIALS Open Access
www.advelectronicmat.de

Tunable Rectification in 2D Porphyrinic Metal–Organic Framework Nanosheets Molecular Heterojunctions

*Bing Huang, Xiaoyu Wang, Chaoguang He, Yongkang Zhang, Pan Qi, Ying Wang, Tong Li, Huixia Fu, Hui Wei, and Cunlan Guo**

As functional electrical devices advance, new strategies for regulating electrical properties are essential for achieving diverse electrical performance. In this study, molecular heterojunction rectifiers are constructed by connecting porphyrinic 2D metal–organic framework (2D MOF) nanosheets and oligophenylene thiols self-assembled monolayers (OPT SAMs) within metal electrodes. The rectification characteristics can be tuned by the molecular length of OPT and the coordinated metal atom in the center of 2D MOFs. Specifically, a rectification ratio of more than 1.67 orders of magnitude is achieved in the heterojunction composed of 2D Zn-TCPP MOF nanosheet (TCCP, tetrakis(4-carboxyphenyl) porphyrin) and OPT3 SAM. Combining Kelvin probe force microscopy measurements and first-principles calculations of the 2D MOF nanosheets, it elucidates that the rectification variations come from the adjustment of energy level alignment at OPT SAMs//2D MOF interface, leading to asymmetric charge transport with the voltage polarities. This strategy can be further extended to Cu-MOF nanosheets, which also exhibit rectification behaviors when placed on OPT2 SAMs. This work provides a universal and flexible strategy for regulating the electrical behaviors of MOFs without the need for specific design and synthesis, paving the way for the development of MOF-based functional electronic devices.

1. Introduction

Metal–organic frameworks (MOFs) are crafted from metal nodes and organic ligands, offering customizable structures, precisely engineered porous structures, large surface areas, and high chemical and thermal stabilities via the selection of specific metal nodes and organic ligands.[1] As a result, the MOFs can be endowed with multiple functionalities. Compared with traditional materials like transition metal dichalcogenides, graphitic, and layered metal oxides, MOFs have unique advantages in applications such as catalysis, gas storage, materials separation, sensors, and biomedicine.[1b,2] As many of these applications ask for proper conductivity of MOFs for good performance, the electrical properties of MOFs have attracted extensive attention.[3] Due to the low conducting or even insulating behaviors of most conventional MOFs, numerous efforts have been focused on the synthetic strategies to improve their conductivity.[4] Moreover, taking advantage of the design flexibility of MOFs in terms of diverse metal nodes as well as organic ligand compositions and structures, emerging applications of MOFs in electronics have been exploited, such as memorizers,[5] field-effect transistors,[6] and switches.[7] These studies demonstrate the versatile functionality of MOFs beyond their use as resistors, extending to capacitors, inductors, and diodes. To further broaden the electronic functions of MOFs, new tactics besides synthetic strategies are desired to regulate the abundant electrical properties of MOFs.

One of the most extensively studied electronic functions is rectification, which exhibits asymmetric current–voltage curves. The rectification of MOFs could be achieved via molecular doping

B. Huang, Y. Zhang, P. Qi, Y. Wang, C. Guo
College of Chemistry and Molecular Sciences
Wuhan University
Wuhan, Hubei 430072, China
E-mail: cunlanguo@whu.edu.cn

The ORCID identification number(s) for the author(s) of this article can be found under https://doi.org/10.1002/aelm.202400773

DOI: 10.1002/aelm.202400773

X. Wang, T. Li, H. Wei
Department of Biomedical Engineering
College of Engineering and Applied Sciences
Nanjing National Laboratory of Microstructures
Jiangsu Key Laboratory of Artificial Functional Materials
Nanjing University
Nanjing, Jiangsu 210023, China

C. He, H. Fu
Center of Quantum Materials and Devices
College of Physics
Chongqing University
Chongqing 401331, China

C. He, H. Fu
Chongqing Key Laboratory for Strongly Coupled Physics
Chongqing University
Chongqing 401331, China

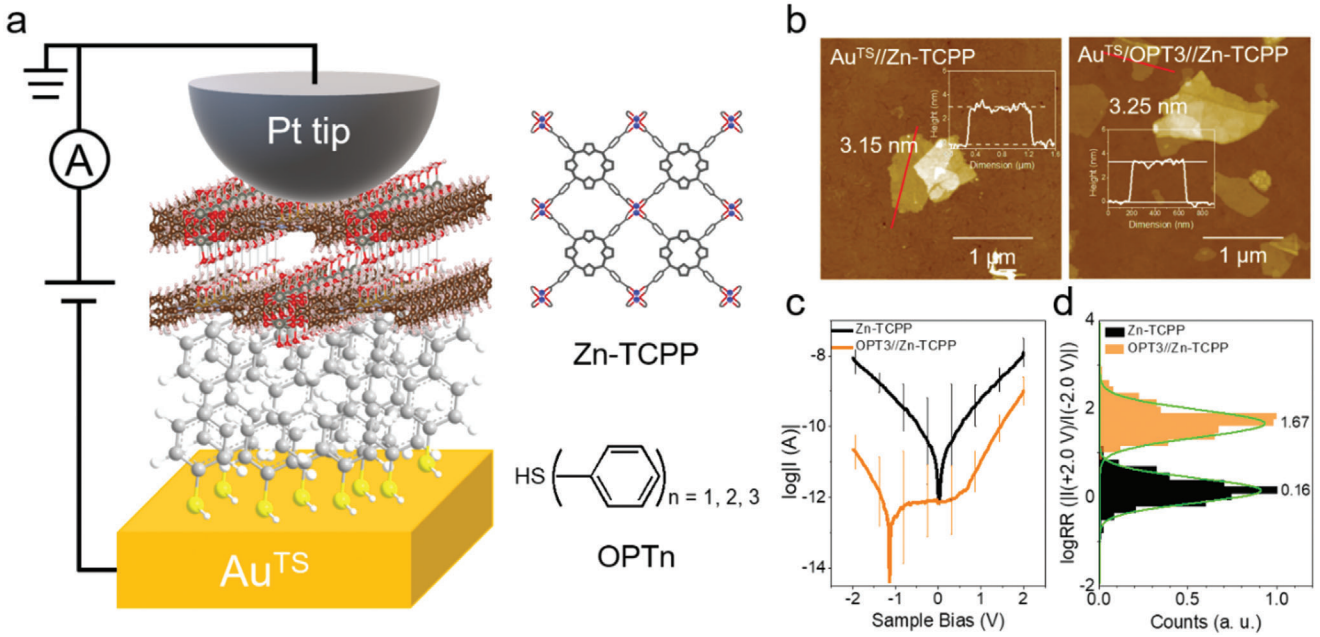

Figure 1. Molecular heterojunction structure. a) Schematic of the electronic measurement for molecular heterojunction by CP-AFM. 2D Zn-TCPP nanosheets are on top of the OPT SAMs on an Au^{TS} substrate (left). The tip loading force is fixed at 2 nN to prevent the damage of the OPT SAMs and 2D MOF nanosheets. The structures of 2D Zn-TCPP and oligophenylene thiol with different benzene ring numbers are shown on the right. b) AFM morphologies of 2D Zn-TCPP nanosheets on Au^{TS} substrate (left) and on top of the OPT3 SAMs (right), respectively. Insets are the height profiles along the red lines. c) Plots of log|I (A)| versus applied bias for the Au^{TS}//Zn-TCPP//PtIr and the Au^{TS}/OPT3//Zn-TCPP//PtIr junctions. The PtIr tip is grounded. d) Statistical histograms of logRR at ± 2.0 V for Au^{TS}//Zn-TCPP//PtIr and Au^{TS}/OPT3//Zn-TCPP//PtIr junctions.

MOFs to p- and n- types and integrating these two types of MOFs in p–n junctions.[8] This requires the delicate design of MOFs. Many rectification phenomena could also be effectively generated through asymmetric energy alignment between molecules and electrodes in response to voltage polarity.[9] Herein, we introduce a novel strategy and design rule for realizing the nanoscale rectification behavior of 2D MOF nanosheets by attaching conjugated molecules and composing the molecular heterojunctions. The rectification properties could be properly modulated via the interfacial energy alignment between 2D MOFs and conjugated molecules. We took porphyrinic 2D MOF nanosheets as a model because their π-conjugated macrocyclic structures endow porphyrinic- or metalloporphyrinic 2D MOFs with good electron transfer properties.[6a,10] With the molecular self-assembly strategy, the molecular heterostructures were composed of porphyrinic 2D MOF nanosheets and oligophenylene thiol (OPT) molecules. Their charge transport behaviors were characterized by the conducting probe atomic force microscopy (CP-AFM). By changing the molecular length of OPT and the type of porphyrinic 2D MOFs, the electrical properties, particularly the rectification behaviors, were regulated in the OPT//2D MOFs heterostructures. Further energy level analysis from Kelvin probe force microscopy (KPFM) characterizations and first-principles calculations helped elucidating the energy level alignments in heterojunctions under applied bias for rectifications. Compared with existing construction methods for heterojunction films (Table S1, Supporting Information), our research establishes a universal and flexible strategy for building nanoscale molecular heterostructure, thereby extending the electrical application region of MOFs in rectification.

2. Results and Discussion

The molecular heterojunction structure is composed of the porphyrinic 2D MOF nanosheets and a molecular SAM on the template stripped gold (Au^{TS}) (**Figure 1a**). By using the CP-AFM with a PtIr-coated AFM tip, the electrical properties of Au^{TS}/SAM//2D MOF//PtIr heterojunctions were recorded. The "/" indicates the Au—S bonding and the "//" represents the non-covalent interface. 2D MOF nanosheets were synthesized by the assembly of tetrakis(4-carboxyphenyl) porphyrin (TCPP) and acetate metal salts (M) (Figure S1, Supporting Information).[11] TCPP with Fe(III) center (TCPP(Fe)) was also used to synthesize 2D MOFs. The 2D MOFs were named M-TCPP and M-TCPP(Fe), where M indicates the corresponding metal salts. The homogeneous distribution of N, O, and metal elements was observed for the 2D MOFs (Figures S2 and S3, Supporting Information). In addition, the crystal structure of 2D MOF nanosheets was characterized by powder X-ray diffraction (XRD), which shows the characteristic diffraction peaks at (110), (002), and (004), respectively, consistent with the literature (Figure S4, Supporting Information).[12] After dropping 2D MOFs dispersion on OPT SAMs, 2D MOFs kept similar morphologies and height with the ones on bare Au^{TS} (Figure 1b; Figures S5–S8, Supporting Information). The height of ≈3.1 nm from AFM imaging indicates three layers of 2D MOFs on OPT SAMs.[13]

In the current–voltage (*I–V*) measurements with CP-AFM, a loading force of 2 nN was applied to prevent sample damage (Figure S9, Supporting Information). This consistent loading force also ensured a comparable contact area between the AFM tip and the 2D MOF nanosheets. More than 160 *I–V* curves

were collected from at least 10 different sample locations of each junction and the average curves were plotted for comparison (Figure 1c). The corresponding histograms of log|I (A)| at +2.0 and −2.0 V along with the Gaussian fits are shown in Figures S10–S12 (Supporting Information). The *I–V* curves for junctions with only 2D MOF nanosheets and OPT SAMs are symmetric though the inconsistent geometry and different Fermi levels of electrodes as well as the polar OPT structure. These factors have little effect on the symmetry of *I–V* curves (Figure 1c; Figure S13d, Supporting Information). When 2D MOF nanosheets are deposited on top of OPT SAMs, the molecular heterojunctions display asymmetric. Typically, a rectification ratio (RR) of 1.67 orders of magnitude is observed for OPT3//Zn-TCPP heterojunction at ± 2.0 V, significantly different from the logRR of 0.16 for Zn-TCPP only junctions (Figure 1d).

The molecular rectification can be further finely tuned by the length of OPT molecules and the composition of porphyrinic 2D MOF nanosheets. As the number of OPT benzene ring increases, the current via the OPTn//Zn-TCPP heterojunctions attenuates (**Figure 2**a). Moreover, the current at negative bias decays more than the current at positive bias, which makes the *I–V* curves asymmetric. The logarithm of current at positive and negative bias both exhibit a linear relationship with the OPT length. The slope for current versus OPT length at positive bias is 0.18 n^{-1}, smaller than the slope of 0.51 n^{-1} at negative bias (Figure 2b). Accordingly, the current variations with OPT length at negative bias are in two orders of magnitude, larger than the current variations at positive bias in OPTn//Zn-TCPP heterojunctions. Both slope values are smaller than the slope of 0.71 n^{-1} for OPT-only junctions, indicating that the possible interactions at OPT and Zn-TCPP interface also participate in the regulation of rectification (Figure S13, Supporting Information). Correspondingly, the logRR values of the heterojunctions are also strongly dependent on the OPT molecular length and are nearly linear with the increasing OPT length (Figure 2c).

The effects of Fe coordination in TCPP on the electrical characteristics of the 2D MOF heterojunctions were then investigated. The *I–V* curves via Zn-TCPP(Fe) alone are symmetric with a current ≈4 times higher than Zn-TCPP (Figure S14, Supporting Information). With OPT SAMs under Zn-TCPP(Fe), the current values of OPTn//Zn-TCPP(Fe) are still larger than that of OPTn//Zn-TCPP heterojunctions though the difference is reduced. Moreover, the trend of current with OPT length at +2.0 V is similar to OPTn//Zn-TCPP heterojunctions, but the trend of current at −2.0 V is different. The *I–V* curves are asymmetric only when OPT3 SAM is under Zn-TCPP(Fe) (Figure 2d). The current measured at −2.0 V bias is ≈1.6 orders of magnitude smaller than that at +2.0 V bias for OPT3//Zn-TCPP(Fe) heterojunction (Figure 2e). The logRR value of the OPT3//Zn-TCPP(Fe) heterojunction reaches 1.64, similar to that of OPT3//Zn-TCPP heterojunction (Figure 2f). In summary, both the OPT molecular length and metal ion coordination in TCPP can control the electrical characteristics of the molecular heterojunctions. In addition, the rectification variation behavior indicates the presence of an interface barrier (Φ_b) caused by the differences in work function between the 2D MOF//OPT SAM heterostructure and the metal electrodes.

To understand the logRR differences among the OPTn//Zn-TCPP and OPTn//Zn-TCPP(Fe) heterojunctions, we further discussed the energy distributions among these heterojunctions. Accordingly, the energy level differences among the heterostructures were evaluated by using KPFM.[14] The contact potential between the PtIr tip and the assemblies on Au^{TS} substrate was measured by KPFM. The contact potential of different lengths of OPT SAMs is from 0.56 to 0.73 V, with slight fluctuations within ≈0.2 V (Figure S15, Supporting Information). It is employed for tuning the work function of the bottom metal electrode. When the Zn-TCPP nanosheets are deposited on OPT SAMs, the contact potential of Au^{TS}/OPT1//Zn-TCPP heterostructures displays a remarkable decrease from 0.56 to 0.15 V compared with OPT1 SAM, and the ones with OPT2 and OPT3 gently increase to 0.65 and 0.76 V. The overall contact potential of the heterostructures increases with the growing number of phenyl groups in OPT (**Figure 3**a; Figure S16, Supporting Information). The highest contact potential, thus highest interface barrier (Zn-TCPP//top PtIr), is observed for the OPT3 heterojunction system, amounting to 0.76 V. These variations in contact potential are likely related to the interactions among OPT, Zn-TCPP, and Au substrate. A larger contact potential measured through KPFM corresponds to smaller work function (Φ). Thus, the Zn-TCPP nanosheet on the OPT SAMs causes the reduction of work function.

The first-principles calculations for the projected density of states (PDOS) of the 2D MOF nanosheets were conducted with the VASP software.[15] A bilayer configuration of 2D MOF was taken as the computational model for easier model construction, with the Au Fermi level normalized to zero as a reference point (Figure S17, Supporting Information). The energy band of the geometry-optimized Zn-TCPP nanosheet is widely spread around the Au Fermi level, suggesting a semiconductor-like behavior with a bandgap of ≈1.10 eV (Figure 3b).[16] The calculated bandgap is smaller than the measured optical bandgap in solution, which is likely due to environmental variations and the inherent tendency of the computational method to underestimate the bandgap (Figure S18, Supporting Information). Here we take the calculated results for the following discussions. Referring to the Fermi level of Au at ≈5.1 eV and PtIr at ≈5.2 eV,[17] the valence band (VB) of Zn-TCPP nanosheet is closer to the Fermi level before interactions with OPT SAMs and electrodes.

Based on the trends of above-measured work function and calculated energy level, the energy level diagrams of the Au^{TS}/OPT//Zn-TCPP//PtIr heterojunctions with an asymmetrical tunneling mode were estimated under applied bias of 0 V, +2.0 V, and −2.0 V (Figure 3d–f).[18] Figure 3d illustrates the energy level diagram at 0 bias, featuring the Fermi level of electrodes, the bandgap and the VB position of 2D MOF nanosheets, and the OPT energy level. There are three interfaces including bottom Au^{TS}/OPT, OPT//Zn-TCPP, and Zn-TCPP//top PtIr tip in the Au^{TS}/OPT//Zn-TCPP//PtIr heterojunctions. As the OPT SAMs form on Au^{TS} via Au—S chemical bonding, the energy level of OPT molecules could shift with Au^{TS} electrode when a bias is applied.[19] When 2D Zn-TCPP nanosheets are on OPT SAMs, the large contact potential changes indicate certain interactions at the interface between the OPT SAM and the 2D Zn-TCPP interface. Therefore, the VB of 2D Zn-TCPP nanosheets would also shift with Au^{TS} electrode under applied bias. The absolute values for the bias-dependent VB shifts are considered to be similar under the positive and negative bias with the same voltages.[14] Based on the above information, at +2.0 V, the VB of the

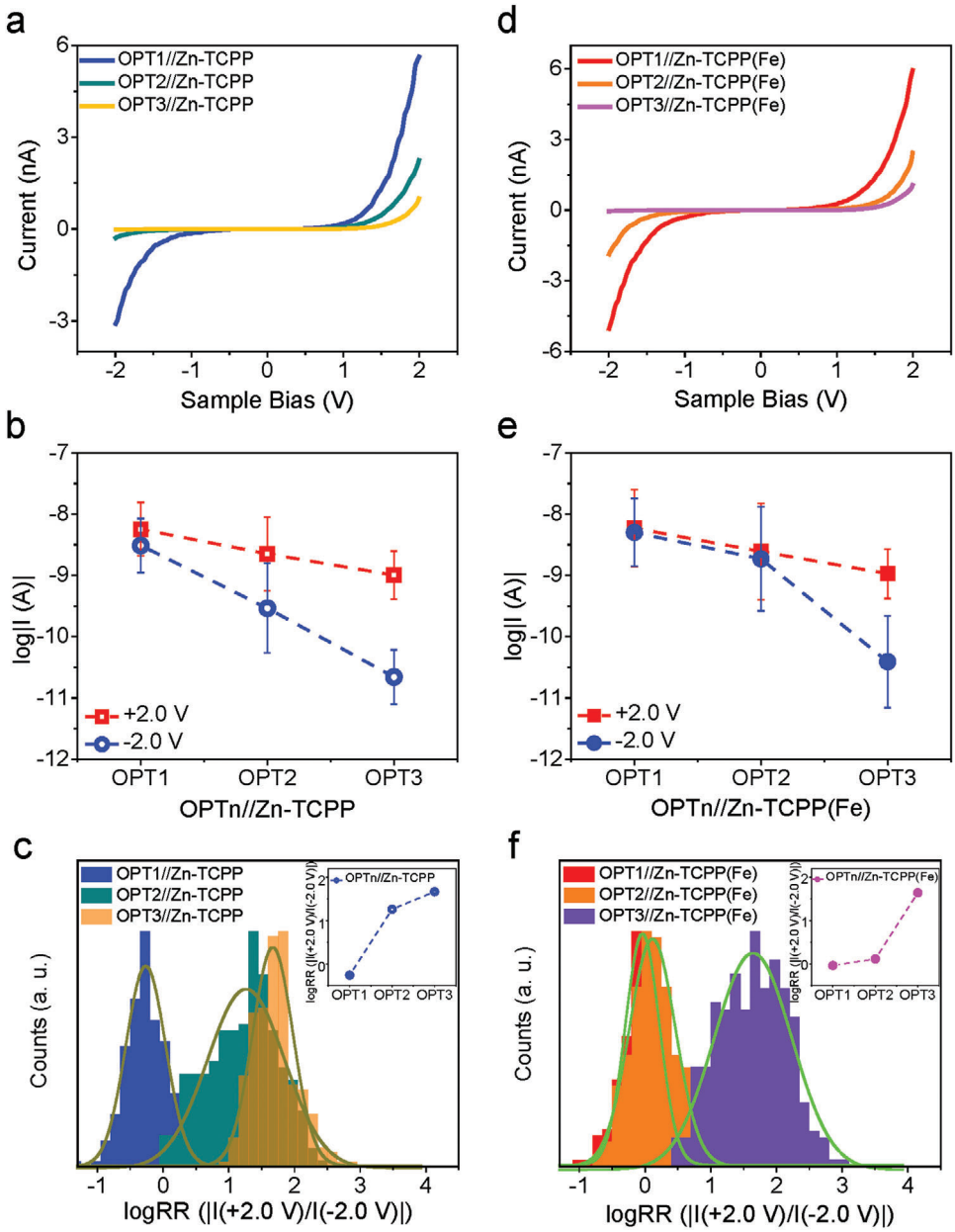

Figure 2. Modulation of rectification for the molecular heterojunctions composed by OPT and porphyrinic 2D MOF. a) Average *I–V* curves for the Au^{TS}/OPTn//Zn-TCPP//PtIr heterojunctions (n = 1, 2, and 3). b) Trends of current at ±2.0 V with OPT molecular length for Au^{TS}/OPTn//Zn-TCPP//PtIr heterojunctions. c) Statistical histograms of logRR (|I(+2.0 V)/I(−2.0 V)|) for the Au^{TS}/OPTn//Zn-TCPP//PtIr heterojunctions. Inset: the relation of logRR with OPT molecular length. d) Average *I–V* curves for the Au^{TS}/OPTn//Zn-TCPP(Fe)//PtIr heterojunctions (n = 1, 2, and 3). e) Trends of current at ±2.0 V with OPT molecular length for Au^{TS}/OPTn//Zn-TCPP(Fe)//PtIr heterojunctions. f) Statistical histograms of logRR (|I(+2.0 V)/I(−2.0 V)|) for the Au^{TS}/OPTn//Zn-TCPP(Fe)//PtIr heterojunctions. Inset: the relation of logRR with OPT molecular length.

Zn-TCPP in Au^{TS}/OPT//Zn-TCPP//PtIr heterojunction shifts downward and lies closer to the Au electrode's Fermi level and facilitates the charge transport (Figure 3e). While at −2.0 V, due to the energy band deviations of Zn-TCPP on different lengths of OPT, the VB of Zn-TCPP on OPT1 would be involved in the potential window, but the VBs of Zn-TCPP on OPT2 and OPT3 slightly exceed the potential window (Figure 3f). The current at −2.0 V becomes smaller than that at +2.0 V and drops differently with the increasing OPT length, as a larger potential drop is required until the Au electrode aligns with the upward shifting transport channel. These energy level variations lead to the rectifications in Au^{TS}/OPT//Zn-TCPP//PtIr heterojunctions, depending on OPT molecular length.

Similarly, the contact potential of Au^{TS}/OPT//Zn-TCPP(Fe) heterostructures was also measured by KPFM. With the OPT length increasing, the contact potential rose from 0.18 to 0.68 V for the OPT//Zn-TCPP(Fe) heterostructures (Figure 3a; Figure S16, Supporting Information). The calculated bandgap for

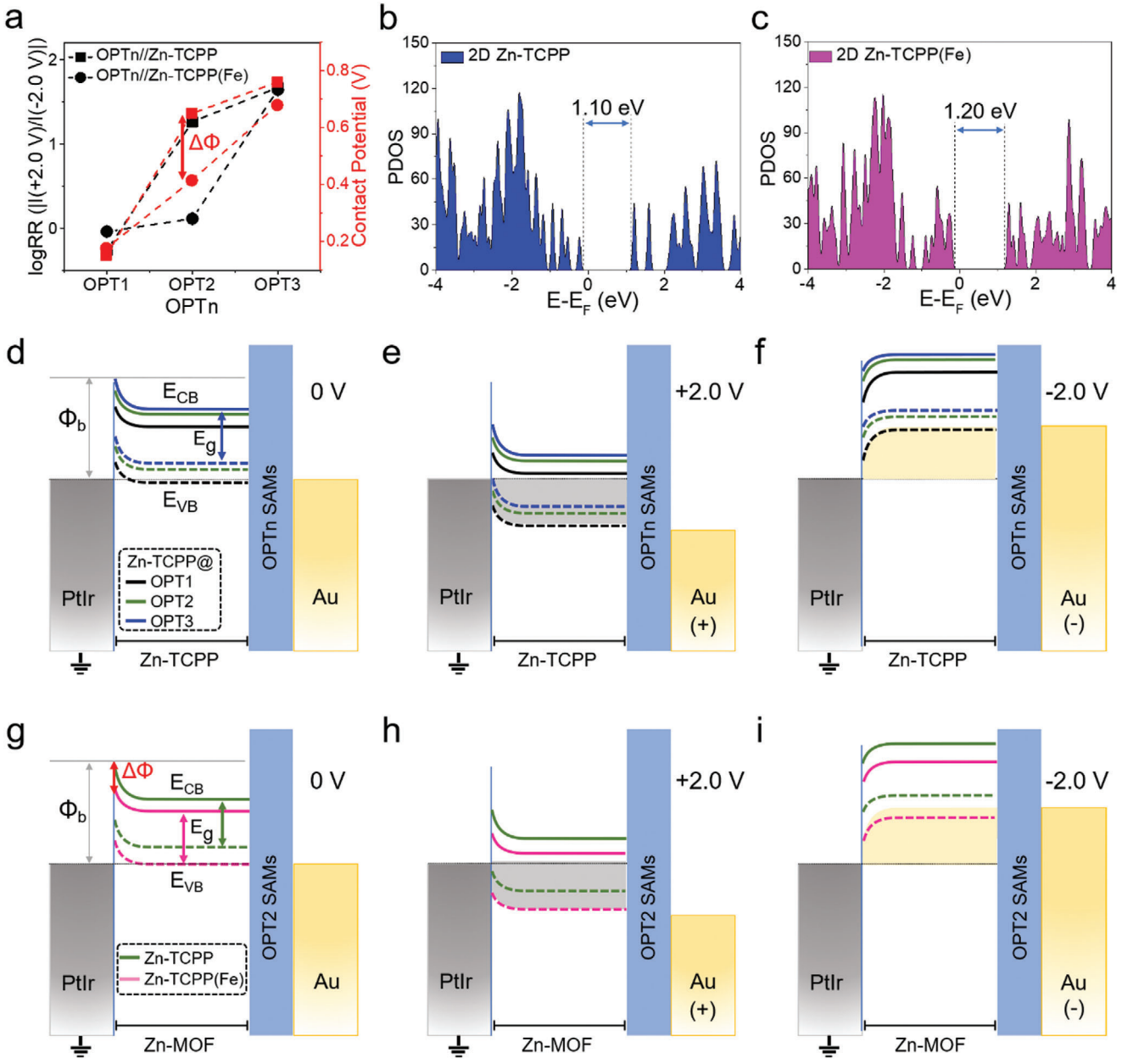

Figure 3. Illustration for the rectification of Au^{TS}/OPTn//2D Zn-MOF//PtIr heterojunctions. a) Relation of logRR (|I(+2.0 V)/I(−2.0 V)|) and contact potential with the OPT molecular length for OPTn//Zn-MOF. b) and c) Calculated PDOS for Zn-TCPP and Zn-TCPP(Fe) nanosheets with the Au Femi level set to zero, respectively. d–f) Schematics of the energy level alignment in Au^{TS}/OPTn//Zn-TCPP//PtIr heterojunctions at the applied bias of 0 V, +2.0 V, and −2.0 V. g–i) Schematics of the energy level alignment in Au^{TS}/OPT2//Zn-MOF//PtIr heterojunctions at the applied bias of 0 V, +2.0, and −2.0 V. n = 1, 2, 3, and Zn-MOF = Zn-TCPP and Zn-TCPP(Fe).

Zn-TCPP(Fe) nanosheet is ≈1.20 eV, which is 0.1 eV larger than that of Zn-TCPP nanosheet (Figure 3c). The VB of Zn-TCPP(Fe) nanosheet adjacent to Au's Fermi level is the primary participant in the charge transport of Au^{TS}/OPT//Zn-TCPP(Fe)//PtIr heterojunctions. Taking Au^{TS}/OPT2//Zn-TCPP(Fe)//PtIr as an example, the energy level diagrams were also drawn at a differently applied bias (Figure 3g–i). The contact potential of OPT2//Zn-TCPP(Fe) is 0.41 V and smaller than OPT2//Zn-TCPP, indicating a larger work function for OPT2//Zn-TCPP (Fe). The VB and conduction band (CB) of Zn-TCPP(Fe) on OPT2 SAM are lower than those of Zn-TCPP (Figure 3g). At both positive and negative bias, the VB of OPT2//Zn-TCPP(Fe) remains within the potential window and closer to the Fermi level of electrodes, facilitating energy level alignment and charge transport (pink dashed lines in Figure 3h,i). This energy level distribution corresponds to a symmetric *I–V* behavior, different from the rectification on Au^{TS}/OPT2//Zn-TCPP//PtIr heterojunction. In a word, the contact potential of OPT//Zn-MOF heterostructures increases with the length of the OPT molecule and fluctuates with the metal coordinated in the TCPP center. These bring various interfacial

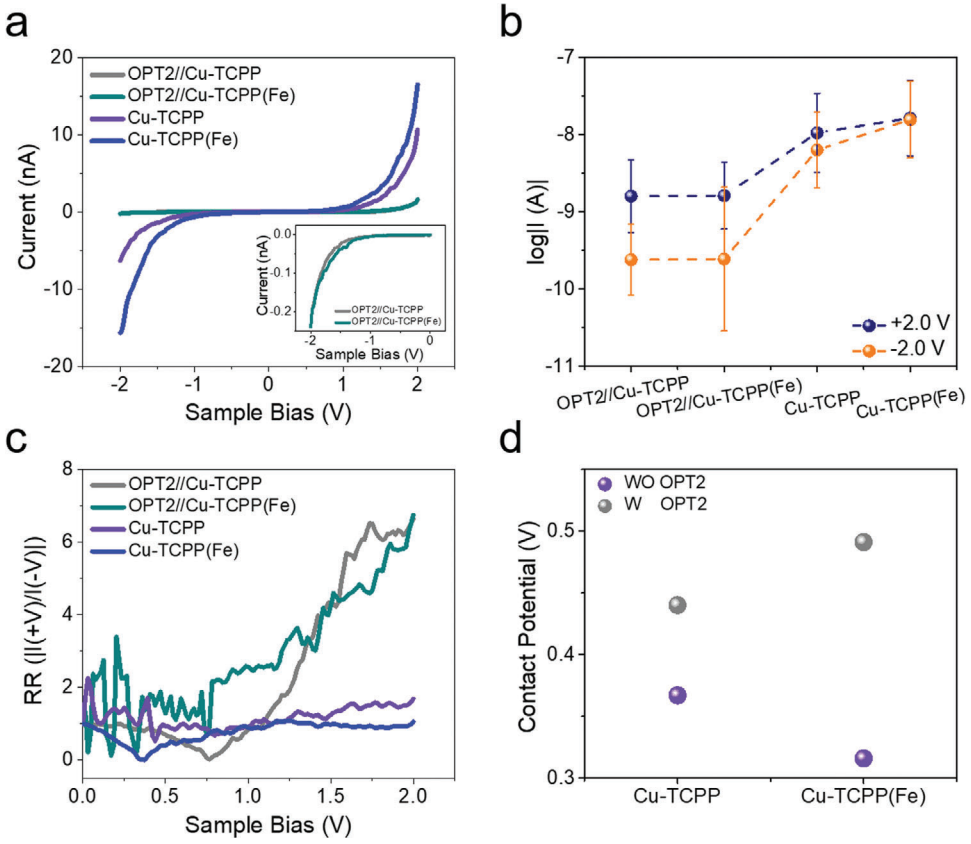

Figure 4. Characterization of the charge transport for the Au^{TS}//2D Cu-MOF//PtIr junctions and Au^{TS}/OPT2//2D Cu-MOF//PtIr heterojunctions. a) Average *I–V* curves for the Au^{TS}//2D Cu-MOF//PtIr junctions and Au^{TS}/OPT2//2D Cu-MOF//PtIr heterojunctions. b) Current measured at ±2.0 V for the Au^{TS}//2D Cu-MOF//PtIr junctions and Au^{TS}/OPT2//2D Cu-MOF//PtIr heterojunctions. c) Plots of the RR versus applied bias (V) for the Au^{TS}//2D Cu-MOF//PtIr junctions and Au^{TS}/OPT2//2D Cu-MOF//PtIr heterojunctions, respectively. d) Contact potential of the 2D Cu-MOF nanosheets on bare Au^{TS} and Au^{TS}/OPT2 SAMs. Cu-MOF = Cu-TCPP and Cu-TCPP(Fe).

energy level alignments under opposite potentials and lead to different rectification behaviors on the Au^{TS}/OPT//Zn-MOF//PtIr heterojunctions.

The aforementioned results prove that our molecular heterojunction strategy can regulate the rectification of porphyrinic 2D Zn-MOF nanosheets. More importantly, our strategy could be further extended to various kinds of 2D MOF nanosheets. For example, we applied the Cu-TCPP and Cu-TCPP(Fe) nanosheets on OPT2 SAMs in the heterojunctions. Compared with the Cu-TCPP and Cu-TCPP(Fe) junctions, both OPT2//Cu-TCPP and OPT2//Cu-TCPP(Fe) also exhibit asymmetric *I–V* curves with smaller current ratios (**Figure 4**; Figure S24, Supporting Information), further demonstrating the modulation ability of OPT SAMs on the rectification of porphyrinic 2D MOF nanosheets. By dropping Cu-TCPP and Cu-TCPP(Fe) on OPT2 SAMs, the current via the heterojunctions drops differently at opposite bias. The current at negative bias is smaller than that at the positive bias, resulting in the rectification (Figure 4b; Figures S22 and S23, Supporting Information). The rectification behavior of Au^{TS}/OPT2//Cu-TCPP//PtIr heterojunction is similar to OPT2//Cu-TCPP(Fe) junction (Figure 4c). From the measured contact potential of both heterostructures and the calculated energy level distribution of Cu-contained 2D MOF nanosheets, the energy levels of Cu-TCPP and Cu-TCPP(Fe) distribute similarly in OPT-modified heterojunctions, which would generate the above indistinguishable rectification results in Cu-contained heterojunctions (Figure 4d; Figures S25–S28, Supporting Information).

3. Conclusion

In this work, we have successfully implemented a molecular heterojunction rectifier composed of porphyrinic 2D MOF nanosheets and OPT SAMs. With CP-AFM, the charge transport behaviors of the heterojunctions were recorded. Around 85 times changes between the lowest and highest rectification ratios (between 0.55 and 46.8) were observed by varying the OPT molecular length and the coordinated metal atom in the center of TCPP in the molecular heterojunctions. Combined with the measured energy level from KPFM and calculated PDOS, the energy level distributions of the heterojunctions were discussed. The asymmetric charge transport behaviors would stem from variations in energy level alignments among 2D MOF, OPT SAMs, and electrodes, depending on the voltage polarities. With the similar strategy, the heterojunctions composed of 2D Cu-MOF nanosheets and OPT2 SAM also exhibit rectification behaviors. This work expands the electrical applications of 2D MOF nanosheets to rectification. By constructing MOF-based heterojunctions with

molecular SAMs, the electronic behaviors for the other types of MOFs with resistance- or rectification-like behaviors may be also flexibly modulated.

Supporting Information

Supporting Information is available from the Wiley Online Library or from the author.

Acknowledgements

The authors thank the financial support from the National Natural Science Foundation of China (Nos. 22374109 and 21974102 to C.G., No. 22374071 to H.W., No. 12104072 to H.F., and No. 22104055 to X.W.), the National Key Research and Development Program of China (No. 2018YFA0703700 to C.G.), the Chongqing Research Program of Basic Research and Frontier Technology, China (No. cstc2021jcyj-msxmX0640 to H.F.), the Doctor "Through Train" Scientific Research Project of Chongqing (No. CSTB2022BSXM-JCX0087 to H.F.). Numerical computations were performed at the Hefei Advanced Computing Center.

Conflict of Interest

The authors declare no conflict of interest.

Data Availability Statement

The data that support the findings of this study are available from the corresponding author upon reasonable request.

Keywords

electrical regulation strategy, metal–organic frameworks, molecular heterojunctions, rectification, self-assembled monolayers

Received: October 5, 2024
Published online:

[1] a) H. Li, M. Eddaoudi, M. O'Keeffe, O. M. Yaghi, *Nature.* **1999**, *402*, 276; b) H. Furukawa, K. E. Cordova, M. O'Keeffe, O. M. Yaghi, *Science.* **2013**, *341*, 974; c) S. Qiu, M. Xue, G. Zhu, *Chem. Soc. Rev.* **2014**, *43*, 6116; d) W. G. Lu, Z. W. Wei, Z. Y. Gu, T. F. Liu, J. Park, J. Park, J. Tian, M. W. Zhang, Q. Zhang, T. Gentle, M. Bosch, H. C. Zhou, *Chem. Soc. Rev.* **2014**, *43*, 5561; e) A. J. Howarth, Y. Liu, P. Li, Z. Li, T. C. Wang, J. Hupp, O. K. Farha, *Nat. Rev. Mater.* **2016**, *1*, 15018; f) Z. Jiang, X. H. Xu, Y. H. Ma, H. S. Cho, D. Ding, C. Wang, J. Wu, P. Oleynikov, M. Jia, J. Cheng, Y. Zhou, O. Terasaki, T. Y. Peng, L. Zan, H. X. Deng, *Nature.* **2020**, *586*, 549; g) G. Lan, Y. Fan, W. Shi, E. You, S. S. Veroneau, W. Lin, *Nat. Catal.* **2022**, *5*, 1006; h) S. Horike, S. Kitagawa, *Nat. Mater.* **2022**, *21*, 983.

[2] a) Y. Peng, Y. Li, Y. Ban, H. Jin, W. Jiao, X. Liu, W. Yang, *Science.* **2014**, *346*, 1356; b) W. Fan, Y. Ying, S. B. Peh, H. Yuan, Z. Yang, Y. D. Yuan, D. Shi, X. Yu, C. Kang, D. Zhao, *J. Am. Chem. Soc.* **2021**, *143*, 17716; c) J. Yang, Y. W. Yang, *Small.* **2020**, *16*, 1906846; d) M. G. Campbell, D. Sheberla, S. F. Liu, T. M. Swager, M. Dinca, *Angew. Chem., Int. Ed.* **2015**, *54*, 4349.

[3] a) L. Sun, M. G. Campbell, M. Dinca, *Angew. Chem., Int. Ed.* **2016**, *55*, 3566; b) G. Zhang, L. Jin, R. Zhang, Y. Bai, R. Zhu, H. Pang, *Coord. Chem. Rev.* **2021**, *439*, 213915; c) R. Saha, K. Gupta, C. J. Gomez Garcia, *Cryst. Growth Des.* **2024**, *24*, 2235.

[4] a) L. Wang, S. E. Saji, L. Wu, Z. Wang, Z. Chen, Y. Du, X.-F. Yu, H. Zhao, Z. Yin, *Small.* **2022**, *18*, 2201642; b) J. Liu, Y. Zhou, Z. Xie, Y. Li, Y. Liu, J. Sun, Y. Ma, O. Terasaki, L. Chen, *Angew. Chem., Int. Ed.* **2020**, *59*, 1081; c) X. Song, X. Wang, Y. Li, C. Zheng, B. Zhang, C.-A. Di, F. Li, C. Jin, W. Mi, L. Chen, W. Hu, *Angew. Chem., Int. Ed.* **2020**, *59*, 1118; d) R. Zhang, J. Liu, Y. Gao, M. Hua, B. Xia, P. Knecht, A. C. Papageorgiou, J. Reichert, J. V. Barth, H. Xu, L. Huang, N. Lin, *Angew. Chem., Int. Ed.* **2020**, *59*, 2669; e) L. E. Darago, M. L. Aubrey, C. J. Yu, M. I. Gonzalez, J. R. Long, *J. Am. Chem. Soc.* **2015**, *137*, 15703; f) M. E. Ziebel, C. A. Gaggioli, A. B. Turkiewicz, W. Ryu, L. Gagliardi, J. R. Long, *J. Am. Chem. Soc.* **2020**, *142*, 2653; g) Q. Mu, W. Zhu, X. Li, C. Zhang, Y. Su, Y. Lian, P. Qi, Z. Deng, D. Zhang, S. Wang, X. Zhu, Y. Peng, *Appl. Catal. B-Environ.* **2020**, *262*, 118114; h) H. Wu, W. Zhang, S. Kandambeth, O. Shekhah, M. Eddaoudi, H. N. Alshareef, *Adv. Energy Mater.* **2019**, *9*, 1900482; i) C. W. Kung, K. Otake, C. T. Buru, S. Goswami, Y. Cui, J. T. Hupp, A. M. Spokoyny, O. K. Farha, *J. Am. Chem. Soc.* **2018**, *140*, 3871; j) A. A. Talin, A. Centrone, A. C. Ford, M. E. Foster, V. Stavila, P. Haney, R. A. Kinney, V. Szalai, F. El Gabaly, H. P. Yoon, F. Leonard, M. D. Allendorf, *Science.* **2014**, *343*, 66.

[5] a) S. M. Yoon, S. C. Warren, B. A. Grzybowski, *Angew. Chem., Int. Ed.* **2014**, *53*, 4437; b) G. Ding, Y. Wang, G. Zhang, K. Zhou, K. Zeng, Z. Li, Y. Zhou, C. Zhang, X. Chen, S. T. Han, *Adv. Funct. Mater.* **2019**, *29*, 1806637; c) L. Liu, J. Dong, J. Liu, Q. Liang, Y. Song, W. Li, S. Lei, W. Hu, *Small Struct.* **2021**, *2*, 2000077.

[6] a) G. D. Wu, H.-L. Zhou, Z. H. Fu, W. H. Li, J. W. Xiu, M. S. Yao, Q. H. Li, G. Xu, *Angew. Chem., Int. Ed.* **2021**, *60*, 9931; b) G. Wu, J. Huang, Y. Zang, J. He, G. Xu, *J. Am. Chem. Soc.* **2017**, *139*, 1360; c) R. Kumar, P. Gupta, S. K. Sharma, *Adv. Mater. Interfaces.* **2021**, *8*, 2100529.

[7] a) R. K. Parashar, P. Jash, M. Zharnikov, P. C. Mondal, *Angew. Chem., Int. Ed.* **2024**, *63*, e202317413; b) S. Roy, M. Das, A. Bandyopadhyay, S. K. Pati, P. P. Ray, T. K. Maji, *J. Phys. Chem. C.* **2017**, *121*, 23803; c) Z. Yao, L. Pan, L. Liu, J. Zhang, Q. Lin, Y. Ye, Z. Zhang, S. Xiang, B. Chen, *Sci. Adv.* **2019**, *5*, eaaw4515.

[8] a) A. Prasoon, B. Dhara, D. Roy, S. Rana, S. Bhand, N. Ballav, *Chem. Sci.* **2019**, *10*, 10040; b) P. Sindhu, N. Ballav, *Inorg. Chem.* **2023**, *62*, 10887; c) A. Chandresh, X. Liu, C. Woell, L. Heinke, *Adv. Sci.* **2021**, *8*, 2001884.

[9] a) X. Chen, M. Roemer, L. Yuan, W. Du, D. Thompson, E. del Barco, C. A. Nijhuis, *Nat. Nanotechnol.* **2017**, *12*, 797; b) J. Shin, S. Yang, Y. Jang, J. S. Eo, T. W. Kim, T. Lee, C. H. Lee, G. Wang, *Nat. Commun.* **2020**, *11*, 1412; c) J. S. Eo, J. Shin, S. Yang, T. Jeon, J. Lee, S. Choi, C. H. Lee, G. Wang, *Adv. Sci.* **2021**, *8*, 2101390.

[10] G. Ding, B. Yang, K. Zhou, C. Zhang, Y. Wang, J. Q. Yang, S. T. Han, Y. Zhai, V. A. L. Roy, Y. Zhou, *Adv. Electron. Mater.* **2020**, *6*, 1900978.

[11] M. Zhao, Y. Wang, Q. Ma, Y. Huang, X. Zhang, J. Ping, Z. Zhang, Q. Lu, Y. Yu, H. Xu, Y. Zhao, H. Zhang, *Adv. Mater.* **2015**, *27*, 7372.

[12] a) X. Liu, Z. Yan, Y. Zhang, Z. Liu, Y. Sun, J. Ren, X. Qu, *ACS Nano.* **2019**, *13*, 5222; b) W. Zhu, Q. Chen, Q. Jin, Y. Chao, L. Sun, X. Han, J. Xu, L. Tian, J. Zhang, T. Liu, Z. Liu, *Nano Res.* **2021**, *14*, 212; c) Y. Zhou, B. Zheng, L. M. Lang, G. X. Liu, X. H. Xia, *ACS Appl. Nano Mater.* **2022**, *5*, 18761.

[13] E.-Y. Choi, C. A. Wray, C. Hu, W. Choe, *CrystEngComm.* **2009**, *11*, 553.

[14] E. Margapoti, J. Li, O. Ceylan, M. Seifert, F. Nisic, A. Tuan Le, F. Meggendorfer, C. Dragonetti, C. A. Palma, J. V. Barth, J. J. Finley, *Adv. Mater.* **2015**, *27*, 1426.

[15] a) G. Kresse, J. Furthmuller, *Phys. Rev. B.* **1996**, *54*, 11169; b) G. Kresse, J. Furthmuller, *Comp. Mater. Sci.* **1996**, *6*, 15.

[16] C. Yang, R. Dong, M. Wang, P. St Petkow, Z. Zhang, M. Wang, P. Han, M. Ballabio, S. A. Braeuninger, Z. Liao, J. Zhang, F. Schwotzer, E.

Zschech, H.-H. Klauss, E. Canovas, S. Kaskel, M. Bonn, S. Zhou, T. Heine, X. Feng, *Nat. Commun.* **2019**, *10*, 3260.

[17] a) B. Kim, S. H. Choi, X. Y. Zhu, C. D. Frisbie, *J. Am. Chem. Soc.* **2011**, *133*, 19864; b) S. Q. Zhou, Y. Q. Liu, Y. Xu, W. P. Hu, D. B. Zhu, X. H. Qui, C. Wang, C. L. Bai, *Chem. Phys. Lett.* **1998**, *297*, 77; c) K. C. Chiu, T. H. Yang, J. M. Wu, *Nanotechnology.* **2013**, *24*, 225602.

[18] P. E. Kornilovitch, A. M. Bratkovsky, R. S. Williams, *Phys. Rev. B.* **2002**, *66*, 165436.

[19] a) Z. T. Xie, I. Baldea, C. E. Smith, Y. F. Wu, C. D. Frisbie, *ACS Nano.* **2015**, *9*, 8022; b) J. Shin, K. Gu, S. Yang, C. H. Lee, T. Lee, Y. H. Jang, G. Wang, *Nano Lett.* **2018**, *18*, 4322.